View Article Online
View Journal

Dalton Transactions

An international journal of inorganic chemistry

Accepted Manuscript

This article can be cited before page numbers have been issued, to do this please use: C. Pazo-Carballo, E. Camu, Y. Hidalgo-Rosa, J. Llanos, X. Zárate, A. B. Dongil, E. Schott and N. Escalona, *Dalton Trans.*, 2025, DOI: 10.1039/D5DT00494B.

This is an Accepted Manuscript, which has been through the Royal Society of Chemistry peer review process and has been accepted for publication.

Accepted Manuscripts are published online shortly after acceptance, before technical editing, formatting and proof reading. Using this free service, authors can make their results available to the community, in citable form, before we publish the edited article. We will replace this Accepted Manuscript with the edited and formatted Advance Article as soon as it is available.

You can find more information about Accepted Manuscripts in the Information for Authors.

Please note that technical editing may introduce minor changes to the text and/or graphics, which may alter content. The journal's standard Terms & Conditions and the Ethical guidelines still apply. In no event shall the Royal Society of Chemistry be held responsible for any errors or omissions in this Accepted Manuscript or any consequences arising from the use of any information it contains.

ROYAL SOCIETY OF CHEMISTRY

rsc.li/dalton

View Article Online
DOI: 10.1039/D5DT00494B

Selective Benzaldehyde/Acetone to benzalacetone Cross-Aldol Condensation Catalyzed by UiO-66 MOFs

C. Pazo-Carballo[a,b,c], E. Camú[b], Y. Hidalgo-Rosa[d], Jaime Llanos[e], X. Zarate[f], Ana Belén Dongil[g], E. Schott[c*], N. Escalona[a,b**]

[a] *Departamento de Química Física, Facultad de Química y Farmacia, Pontificia Universidad Católica de Chile*

[b] *Departamento de Ingeniería Química y Bioprocesos, Escuela de Ingeniería, Pontificia Universidad Católica de Chile*

[c] *Departamento de Química Inorgánica, Facultad de Química y de Farmacia, Pontificia Universidad Católica de Chile.*

[d] *Centro de Nanotecnología Aplicada, Facultad de Ciencias, Ingeniería y Tecnología, Universidad Mayor, Santiago, Chile.*

[e] *Departamento de Química, Facultad de Ciencias, Universidad Católica del Norte, Avda. Angamos 0610, Antofagasta 1270709, Chile*

[f] *Instituto de Ciencias Aplicadas, Facultad de Ingeniería, Universidad Autónoma de Chile.*

[g] *Instituto de Catálisis y Petroleoquímica, CSIC, Cantoblanco, 28049 Madrid, España.*

**maschotte@gmail.com, edschott@uc.cl*

***neescalona@uc.cl*

Abstract

The cross-aldol condensation reactions are an important family of reactions that generate added value chemicals with long chain products. Those products have multiple applications, such as pharmaceutical industry, flavors and fragrances, agricultural chemicals and fine and specialty chemicals, among others. Possible products are long chain aromatic compounds, which could be used to generate fuels. The ability to generate that kind of fuel from biomass has been a challenge in the last years. In this report the cross-aldol condensation reaction study using a family of UiO-66 MOFs between benzaldehyde and acetone to produce benzalacetona was performed. Thus, a family of UiO-66 MOFs was synthetized, characterized (by means of N_2 physisorption, NH_3-TPD, CO_2-TPD, ATR-FTIR, and powder X-ray diffraction) and its catalytic activity was studied in

View Article Online
DOI: 10.1039/D5DT00494B

detail. A good conversion and selectivity were obtained. A thorough study of the kinetics of this reaction was performed for all the used UiO-66 MOFs. In this sense, the Langmuir–Hinshelwood kinetic models fitted the experimental data. The behavior predictions using different metals (Zr, Hf or Zr/Hf) and linkers (BDC or PDC) were fitted from the bimolecular one-site and two-site models. Competitive and non-competitive mechanisms were used to explain the production of the main intermediate compound (β-hydroxy ketone). The catalyst Zr/Hf-UiO-66 showed the best activity, which could be attributed to the greater total interaction energy of benzaldehyde/acetone on the catalyst surface (as shown by DFT calculations). A synergetic effect is observed for the bimetallic UiO-66 catalyst between Zr and Hf, obtaining a higher reaction rate than for the monometallic catalysts. Furthermore, a similar effect was reflected in the TOF for Zr/Hf-UiO-66. The best selectivity towards benzalacetone was obtained for Hf-UiO-66-PDC at iso-conversion conditions. Finally, depending on the metal-linker pair, differences in the benzaldehyde/acetone adsorption modes were observed, indicating the presence of bimolecular kinetic adjustments at one and two sites for the aldol condensation of benzaldehyde. All the results herein shown were supported by means of DFT calculations.

Keywords: Metal-Organic Frameworks, Cross aldol condensation, Benzaldehyde, Langmuir-Hinshelwood, benzalacetone.

1. Introduction

Metal-organic frameworks (MOFs) are hybrid molecules synthesized from metal ions and organic ligands (linkers) that form three-dimensional structures with high porosity and thermal and chemical stability.[1] Given the many combinations that can be made between metals and linkers, it is possible to develop MOFs with specific characteristics, which has allowed using these compounds for several years in different applications.[2,3]

A variety of catalytic reactions have been investigated using MOFs. Examples of organic chemical reactions that have been reported include condensation,[4] acetylations,[3] cycloaddition,[5] isomerization,[6] and hydrogenation.[6] Specific fine chemicals can be produced using MOF-based materials as effective catalysts.[7] Considering practical applications, recent research has focused on thermally and chemically stable MOFs, where Zr-MOFs are remarkably stable. [8,9] Due to their unique qualities, Zr-MOFs are valuable materials that make attracting candidates for heterogeneous catalysis, as catalysts or as supports for catalysts.[10] On the other hand, Hafnium-

View Article Online
DOI: 10.1039/D5DT00494B

based MOFs, which have outstanding thermal and chemical stability (similar to zirconium-based MOFs), have received considerably less attention. One of the frameworks that shows most of the previously mentioned characteristics corresponds to the UiO-66 MOF. UiO-66 (UiO = University of Oslo) consists of zirconium clusters ($Zr_6O_4(OH)_4$) as building units and organic linkers of 1,4-benzenedicarboxylate (BDC).[8] The metals or linkers could be changed, maintaining the MOF structure, but changing its properties (such as catalytic activity or porosity).[8]

It has been demonstrated that terephthalate defects are responsible for the UiO-66 material's catalytic activity in Lewis acid-catalyzed processes.[11,12] Furthermore, by replacing 1,4-benzenedicarboxylate with the 2,5-pyridinicarboxylate (PDC) ion linker, multiple isoreticular structures of UiO-66 may be produced. This would allow for the incorporation of more hydrophilic linker molecules, which would increase the amount of water that was absorbed by the reaction medium.[11,13–15] These modifications significantly alter the active site's characteristics and have an impact on the thermal and chemical stability. It was demonstrated by Lescouet *et al*.[16] that the catalytic activity can be tuned by replacing the linkers which modifies the Brønsted acidity.

There are several reports of the catalytic activity in the UiO-66 MOF for reactions such as aldol condensation,[11] Knoevenagel condensation,[17] Claisen-Schmidt condensation,[18] among others.

Aldol condensation is a widely used strategy to increase molecular size and generate added-value derivatives of biomass waste. Benzalacetone can be obtained from the reaction between benzaldehyde and acetone as a product. Benzalacetone has been shown to be essential in manufacturing added-value chemicals used in the pharmaceutical and food industries, as well as biofuels.[19] This reaction, particularly the benzaldehyde coupling condensation reaction, has been studied using homogeneous[20,21] and heterogeneous catalysts.[22,23] However, low yields and poor selectivity have been obtained [22,23]. Due to the MOF's versatility, these materials have been used as heterogeneous catalysts for this reaction in recent years.[24–26] The use of Zr-UiO-66 and Hf-UiO-66 as heterogeneous catalysts in aldol condensation has been investigated. However, no study has been performed on the electronic synergistic Zr/Hf interactions in the cluster and their impact on the catalytic performance of the process. As well as the influence of changing the hydrophilic character of the organic linkers containing PDC groups. To the best of our knowledge, the complete mechanism of the surface response has not yet been resolved. In addition, there is an ongoing need to generate novel and efficient catalysts to produce biofuels from biomass derivatives.

View Article Online
DOI: 10.1039/D5DT00494B

In this work, the cross-aldol condensation of benzaldehyde with acetone as a solvent-producing benzalacetone catalyzed by M-UiO-66-BDC (with M=Zr, Hf, and Zr/Hf) and M-UiO-66-PDC (with M=Zr and Hf) was carried out. Both families of MOFs were synthesized and characterized by N_2 physisorption using the BET Rouquerol method, NH_3-TPD, CO_2-TPD, ATR-FTIR, and powder X-Ray diffraction. The cross-aldol condensation reaction was studied in a batch reactor at 5.5 bar under N_2 and 383 K. Furthermore, DFT studies were carried out to support the catalytic results. Finally, the kinetics of the reaction was studied in detail fitting the experimental results with bimolecular one and two sites Langmuir-Hinshelwood (L-H) mechanism.[27]

Experimental

Zr-, Hf-, and Zr/Hf-UiO-66-BDC synthesis

The three UiOs with BDC as linker were synthesized using the procedure previously published by Farha *et al.*[28] A 20 mL vial was loaded with $ZrCl_4$ (125 mmol), 7.5 mL of DMF, and 1 mL of concentrated HCl before being sonicated for 20 minutes until fully dissolved. Finally, the linker (125 mmol) and another 7.5 mL of DMF were added, and the mixture was heated at 353 K overnight. In the case of the mixed metallic MOF (Zr/Hf-UiO-66-BDC), the metallic precursors $ZrCl_4$ and $HfCl_4$ were used in a 1:1 proportion (62.5:62.5 mmol).

Zr- and Hf-UiO-66-PDC synthesis

Zr- and Hf-UiO-66-PDC were prepared under Stock *et al.*[29] procedures (see ESI† for further information). All products were separated and washed by centrifugation at 8000 rpm for 10 min with their solvent (2x10 mL) and then with ethanol (2x10 mL). Finally, the obtained solids were dried under vacuum at room temperature for five days.

Characterization of MOFs

The catalysts were characterized by N_2 physisorption, powder X-ray diffraction, temperature-programmed ammonia desorption (NH_3-TPD), temperature-programmed CO_2 desorption (CO_2-TPD), and infrared spectroscopy (more experimental details can be found in the supplementary materials †).

Computational details

View Article Online
DOI: 10.1039/D5DT00494B

This study presents a series of calculations to explore the interactions between benzaldehyde and acetone with the material, *i.e.,* M-UiO-66-BDC or M-UiO-66-PDC. The interactions of acetone and benzaldehyde on material defects acidic sites have been investigated. Based on previous works discussed in the literature, the simulation was carried out by extracting a finite fragment of the MOFs (cluster model).[30] This method allows the simulation of a material's electronic properties through theoretical approaches and methodologies available in molecular software. In the herein report, a cluster model consistent with a single node $[M_6O_4(OH)_4]^{12-}$ was used (three complete linkers, seven truncated linkers, and considering only one defect or vacancy).[31] To be more specific, the structure of the cluster model is comprised of the fragment $[M_6O_4(OH)_4(Linker)_3(HCOO)_8]$, with M representing Zr^{4+} and Hf^{4+}, while linker referring to BDC or PDC. In contrast, one of the linker sites is vacant due to the consideration of a defect in the structure. Please refer to Fig. S1† for visual representation. The proposed structural model for the bi-metallic UiO-66 systems is composed of the fragment $[Zr_3Hf_3O_4(OH)_4(BDC)_3(HCOO)_8]$.

All calculations were carried out in the framework of the Density-functional theory (DFT) method using the Amsterdam Density Functional (ADF 2023) software package.[32] The relativistic effects due to the presence of Zr or Hf can play a crucial role in the material's chemical and physical properties.[33] Thus, considering the relativistic effects is essential for accurately describing a work's interest properties. All simulations incorporated the relativistic effects using the zeroth-order regular approximation (ZORA).[34] The optimization of all structures was performed utilizing the Minnesota density M06-L functional, [35] along with the standard Slater-type orbital basis set and two additional polarization functions (STO-TZ2P). [36] In order to study the interaction between the systems M-UiO-66/acetone and M-UiO-66/benzaldehyde, the energy decomposition analysis (EDA) was employed using the Morokuma-Ziegler scheme. [37] The EDA analysis was performed using the meta-hybrid Functional (10% HF exchange) by Tao-Perdew-Staroverov-Scuseria TPSSH functional[37] at the TZ2P/ZORA level of theory. Equation 1 demonstrates the breakdown of the interaction energy ($\mathbf{\Delta E_{Int}}$) in this analysis.

$$\Delta E_{Int}=\Delta E_{Pauli} + \Delta E_{Elec} + \Delta E_{Orb} + \Delta E_{Disp} \quad (1)$$

The term $\mathbf{\Delta E_{Pauli}}$ accounts for the repulsive interaction between the occupied orbitals of both fragments.[38] The second term, $\mathbf{\Delta E_{Elec}}$, considers the traditional electrostatic interaction between the two fragments.[31] The third term, $\mathbf{\Delta E_{Orb}}$, encompasses interaction involving molecular orbitals

View Article Online
DOI: 10.1039/D5DT00494B

associated with charge transfer, polarization, and other factors. [39] The term $\mathbf{\Delta E_{Disp}}$ represents the contribution of dispersion force.[40] In this analysis, Grimme's D3 dispersion correction was employed to properly account for the dispersion forces in EDA computations.[41] This correction allows for the inclusion of weak interactions between the fragments.

Furthermore, the analysis of orbital contribution was performed using the natural orbital of chemical valence (NOCV) approach introduced by Mitoraj.[42] The scheme considers the interaction of a system AB (with the wavefunction ψ AB) through the interaction of its individual fragments. NOCV analysis serves to identify the charge-flow channels, breaking down the overall change in density $\mathbf{\Delta\rho}$. Equation 2 represents the NOCV by adding the total of pairs of complementary eigenfunctions (ψ-k, ψk) associated with the eigenvalues v_k and $-v_k$. The absolute values of these eigenvalues are equal, but their signs are opposite. [43]

$$\Delta\rho_{\mathrm{orb}}(r) = \pi r^2(r) = \sum_{k=1}^{N/2} \Delta\rho_{\mathrm{k}} v_{\mathrm{k}} \left[-\psi_{-k}^2(r) + \psi_k^2(r) \right] = \sum_{k=1}^{N/2} \Delta\rho_{\mathrm{k}}(r) \qquad (2)$$

The molecular fragments establish charge-flow channels, which are determined by complementary pairs of NOCV. Within each $\Delta\rho_{\mathrm{orb}}(\mathrm{i})$, electron density can be calculated for both outflow and inflow, denoted as $\Delta\rho_{\mathrm{orb}}$ [outflow(i)] and $\Delta\rho_{\mathrm{orb}}$ [inflow(i)], respectively. These calculations are based on pairs of NOCVs ($\psi_{-\mathrm{k}}$, ψ_{k}) with identical absolute eigenvalues $|v_{\mathrm{k}}|$. Equation 4 allows for the examination of these terms individually. The focus is specifically on the processes of electron density outflow and inflow from a particular fragment. [38,44]

$$\Delta\rho_{\mathrm{orb}}(r) = \sum_{k=1}^{N/2} \left[\Delta\rho_{orb}^{outflow}(i) + \Delta\rho_{orb}^{inflow}(i) \right] \qquad (3)$$

The counterpoise approach was utilized to adjust the interaction energies due to the basis set superposition error (BSSE). [45]

Catalytic activities

The UiO-66 (mono- and bimetallic) were activated before the catalytic test by drying the materials under vacuum at 453 K overnight in Micromeritics SmartVacPrep equipment. The Aldol condensation was carried out at 383 K and 5.5 bar of nitrogen in a 20 mL batch reactor (Parr Model 4590) charged with 20 mg of the catalyst in 15 mL (247 mmol) of acetone, 0.60 mL of benzaldehyde and 0.445 mL (0.273 mmol) of n-dodecane as internal standard. The reaction mixture was then stirred at 700 rpm for four hours. Reaction conversion was monitored by taking

View Article Online
DOI: 10.1039/D5DT00494B

aliquots (~200 μL) from the reaction mixture at different time intervals and analyzed by gas chromatography (GC) in a Shimadzu GC-2030 provided with a flame ionization detector (FID) equipped with an Elite-1 column (Perkin Elmer, 30 m×0.32 mm, film thickness of 0.25 μm). Conversion and product selectivity were defined according to equations 4 and 5, respectively:

$$Conversion\ (\%) = \frac{n_{products}}{n_{reagent\ remaining} + n_{products}} . 100 \quad \text{(Equation 4)}$$

$$Selectivity\ (\%) = \frac{n_{product\ i}}{\Sigma n_{products}} . 100 \quad \text{(Equation 5)}$$

The initial reaction rate r_0 (mol g^{-1} s^{-1}) was calculated from the initial slope (b) of the conversion vs. time plot (s^{-1}) according to equation 6, where m (g) represents the mass of the catalyst.

$$r_0 = \frac{b\ x\ n^0_{benzaldehyde}}{m} \quad \text{(Equation 6)}$$

The mass balance was performed by comparing the conversion of benzaldehyde disappearance with the analyzed products, showing a value superior to 80% in all the measurements.

Kinetic modeling

A rate expression that included the concentrations of benzaldehyde (Bal), benzalacetone (B-One), beta hydroxy acetone (B-ol), and acetone (Ac), based on the conventional bimolecular L-H one and two active sites mechanisms, was used to fit the experimental results. A nonlinear residual sum of squares (RSS) regression analysis of the differences between the observed and calculated values was used to provide the experimental data simultaneously. To ensure that the fitting resulted in the global minimum, different initial assumptions of the adjustable parameters ensured that the program always converged to the same minimum with the same fitting parameters for other initial guesses, as previously reported.[46]

3 Results and Discussion

3.1 MOF's characterization

View Article Online
DOI: 10.1039/D5DT00494B

The nitrogen isotherm exhibits the characteristic microporous structures type-I form according to the IUPAC report[47] (see Fig. S2 ESI†). The N_2 adsorption-desorption analysis allowed the evaluation of BET surface areas (S_{BET}), total (V_t), mesoporous (V_m), and micropore volumes (V_0) of mono- and bimetallic UiO-66 catalysts, and these results are summarized in Table 1. The study of the textural properties of UiO-66-BDC revealed that all these materials presented similar BET surface areas. Additionally, Fig. S2 of the ESI shows a change in the mesoporous zone of the isotherm for UiO-66-PDC due to the possible formation of mesopores or an interaction adsorbate-adsorbent with the free electron pairs of pyridinic nitrogen. According to the pore volume study, all mono- and bimetallic-UiO-66 MOFs have a total pore volume of more than 0.45 $cm^3\ g^{-1}$. A plot of the pore size distributions (PSD) against pore width is shown in Fig. S3.† The PSD for all UiO-66 synthesized were calculated by applying the NLDFT method from the desorption branch of the N_2 isotherms. Mono and bimetallic UiO-66 MOFs displayed a pores distribution that corresponds to the two types of cavities present in the microporous structure of this material, which has been described as octahedral (≈11 Å) and tetrahedral (≈8 Å) cavities connected via triangular-shaped windows (≈6 Å), consistent with the previous report.[48] On the other hand, the pore size distribution of MOFs containing PDC is distorted. A reduction in the octahedral pore is found for Zr-UiO-66-PDC, but a broadening of the pores is reported for Hf-UiO-66. The nature of the synthesis probably causes textural alterations in both materials.

Table 1. Textural properties of MOFs.

Compound	S_{BET} ($m^2\ g^{-1}$)	V_0 ($cm^3\ g^{-1}$)	V_m ($cm^3\ g^{-1}$)	V_t ($cm^3\ g^{-1}$)
Zr-UiO-66-BDC	1377	0.51	0.08	0.59
Zr-UiO-66-PDC	1083	0.42	0.14	0.56
Zr/Hf-UiO-66-BDC	1325	0.51	0.06	0.57
Hf-UiO-66-BDC	934	0.38	0.12	0.46
Hf-UiO-66-PDC	601	0.16	0.29	0.45

In order to evaluate the crystalline structure feature for all MOFs Fig. 1 shows the XRD patterns. According to the reference XRD pattern obtained by Cavka *et al* and Camú, *et al*,[8,49] it was observed that all the materials present agreement in the diffraction patterns, suggesting a UiO-66

View Article Online
DOI: 10.1039/D5DT00494B

isostructural framework topology (fcu) for all the synthesized MOFs (mono and bimetallic) in agreement with the literature.[49] Furthermore, an X-ray diffraction pattern of Zr-UiO-66 as a reference material was compared to the bimetallic Zr/Hf-UiO-66 sample to confirm that it displayed a pattern resembling that reported by Rogge et al.[50]

For the FT-IR spectroscopy study shown in Fig. S4†, the main differences between the structures are observed for the vibrations at 555, 660, and 740 cm^{-1} for mono- and bimetallic UiO-66 MOFs. These vibrations correspond to the μ_3-OH, μ_3-O and, M-OH bonds stretching found in the secondary building unit (SBU) of each MOF [51,52]. The bands between 1506 and 1589 cm^{-1} correspond to the terephthalic acid ligands' C=C vibrational mode. The C-O stretching mode was allocated to the strong bands at ≈1393 cm^{-1}, and the distinctive band at ≈1664 cm^{-1} was attributed to the C=O vibrational mode in UiO-66. In addition, the produced PDC MOFs exhibit the disubstituted pyridine group's C=C vibrational mode, with vibrations between 1400 and 1594 cm^{-1}. Three weak bands linked to the pyridine's distinctive C-N bond can be observed between 1025 and 1200 cm^{-1}.

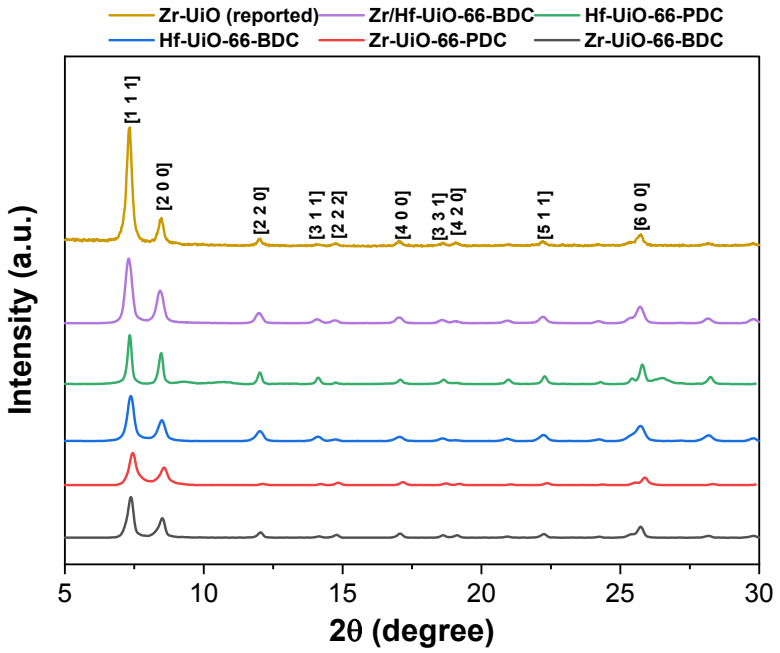

Fig. 1. XRD patterns obtained for UiO-66's. [8,49,50]

View Article Online
DOI: 10.1039/D5DT00494B

With the aim of determining the organic linker vacancies in the prepared MOFs, potentiometric acid-base titration and thermogravimetric analysis were performed, see Table S1†. All the studied MOFs showed linker vacancies, suggesting that all MOFs have high concentrations of acid sites. The generation of acid sites can be related to the inductive effect caused by the oxophilic nature of the metal cluster's atoms in the SBU. Additionally, at least three types of protons generated by water adsorption in the vacancies produced by the absence of linker (μ_3-OH, -OH_2, and -OH) are observed in Fig. S5†. [53] Acid-base titration of both mono- and bimetallic UiO-66 reveals curves with three inflection points associated with the three types of protons. However, the defects or vacancies of 2,5-pyridinecarboxylate linkers were calculated using TGA, as reported by Valenzano *et al.* [54] showing that Zr-UiO-66-PDC presents the highest number of defects with respect to the other MOFs with pyridine group in the linker molecule (Fig. S6-S7†).

To get information about the type and nature of acid site over the different UiO-66 samples, temperature-programmed ammonia and carbon dioxide desorption was performed, followed by mass spectrometry (NH_3-TPD-MS and CO_2-TPD). The mass fragment 17 m/z was monitored while heating the MOFs from 100 to 450°C, which indicates NH_3 binding to multiple sites. In Fig. S8a†, the behavior for NH_3 desorption temperature can be observed, demonstrating that all the catalysts displayed one single contribution according to maxima in the range from 124 to 254 °C. The distinct low-temperature desorption peak is attributed to NH_3 coordinated to weak acidic sites of different TPD profiles.[55] After deconvolution of the NH_3 desorption peak (see Fig. S8b-f†), it was shown that MOFs using BDC as a linker include acidic sites below 150 °C, which might be ascribed to the creation of an NH_3 hydrogen bond in the μ3-OH of the metal cluster. Above 150 °C, two peaks indicative of weak acid sites are detected. The overall quantity of acid in the heated MOFs and their derivatives may be represented as the amount of NH_3 bound to the acid sites, which was calculated by subtracting the amount of physically adsorbed and hydrogen-bonded NH_3 from the total amount of NH_3. Table 2 shows the amounts of acid sites for all MOFs, with a higher concentration observed for Zr/Hf-UiO-66 preceded by monometallic UiO-66. Regarding the MOFs with PDC as a linker, the presence of a fourth peak is observed, which could be attributed to the formation of a pyridinium ion resulting from the protonation of pyridinic nitrogen.

Figure S9† depicts the CO_2 desorption patterns of all materials tested following activation at 180°C. The desorbed quantities are presented in Table 2. A very modest CO_2 adsorption was

View Article Online
DOI: 10.1039/D5DT00494B

observed for the conditions used for MOFs containing BDC. On the other hand, MOFs with PDC exhibit a distinct peak located around 115-150°C with varying intensities and a weak shoulder at higher temperatures (185°C). All materials showed weak basic sites with no distinction associated with the change of organic linker.

Table 2. Concentration of total acidic and basic sites in MOFs determined by TPD-NH_3 and TPD-CO_2

Materials	Total acid sites amount. (mmol g^{-1})	Total basic sites amount. (mmol g^{-1})
Zr-UiO-66-BDC	1.08	0.13
Hf-UiO-66-BDC	1.14	0.07
Zr/Hf-UiO-66-BDC	1.26	0.10
Zr-UiO-66-PDC	0.74	0.26
Hf-UiO-66-PDC	0.61	0.12

The XPS data provide details on the surface constituents of the material and the binding energies of the elements that make up the MOFs. Fig. S10† shows that Zr/Hf-UiO-66 contains Zr3d, Hf4f, C1s and O1s elements. The spectrum of Zr3d has two Zr peaks ($3d_{3/2}$ and $3d_{5/2}$) located at 185.2 eV and 182.8 eV, respectively, indicating the existence of Zr^{4+} in O-Zr-O,[56] this being previously confirmed by FTIR-ATR. The Hf4f spectra shows two main peaks at binding energies of 17.5 and 19.1 eV, corresponding to the two Hf peaks ($4f_{7/2}$ and $4f_{5/2}$), respectively. Whereas the three peaks found in the XPS spectrum of C1s at 284.7, 286.5 and 288.8 eV are attributed to C-C, C=C and O-C-O groups, respectively. These types of bonds are characteristic of the carboxylate group and aromatic ring of the organic linker. While the XPS spectrum of O1s shows three main peaks which were located at 530.5, 532.1 and 533.5 eV. The first one is characteristic of metal-oxygen bonds and the other two are distinctive of oxygens corresponding to C=O and C-O bonds of the organic linker. The theoretical binding energies for Zr3d and Hf4f show values of 182.3 eV and 18.3 eV for the M-O bond respectively. XPS analysis of bimetallic UiO-66 revealed an atomic ratio for Zr/Hf-UiO-66 that was almost 1:1 (see Table S2). This suggests that there are three Zr and three Hf atoms in the MOF metal cluster as reported in the literature.[8]

View Article Online
DOI: 10.1039/D5DT00494B

On the other hand, XPS analysis shows a small shift (>0.5 eV) for the binding energy of Zr 3d and Hf 4f present on the surface of bimetallic UiO-66 (see Fig. S10†). This evidence suggests an electronic interchange when both metals are present in the metal cluster of UiO-66. Therefore, it could improve the cooperative effect that allows for predicting an enhancement in catalytic activity.

3.2 Theoretical results

The M-UiO-66/**Bal** and M-UiO-66/**Ac** systems were initially studied using the host/guest interaction models (where **Bal** represents benzaldehyde and **Ac** corresponds to acetone). These models consider the interaction between the host (M-UiO-66) and the guest molecules (**Bal** or **Ac**) on defect sites generated by a missing linker. According to the results of the geometry optimization, it is observed that in the M-UiO-66-PDC or M-UiO-66-BDC systems, the **Bal** and **Ac** exhibit a final conformation in closer proximity to the Lewis (M) and Brønsted (μ_3-O) acid sites. The optimized geometries of the Hf-UiO-66-BDC/**Bal** and Zr-UiO-66-BDC/**Bal** systems at the ground electronic state (S_0) can be seen in Fig. S11 of the ESI.† For these intermolecular interactions, the calculated length Hf···OHC- and Zr···OHC- are 2.27 and 2.29 Å, for Hf-UiO-66-BDC/**Bal** and Zr-UiO-66-BDC/**Bal** respectively, see Table S3†. For these systems, the angles of C−O···Hf and C−O···Zr are 142° and 130°, respectively, which is commonly found for the C=O···M interaction.[57] The Zr/Hf-UiO-66-BDC/**Bal** system exhibits optimized structures in the S_0 electronic state that closely resemble the arrangement found in the monometallic-UiO-66 systems. The bimetallic-UiO-66-BDC exhibits a geometric arrangement where the interacting system demonstrates that **Bal** interacts with the Hf metal center at the defective site. The intermolecular interaction is characterized by a distance Hf···OHC- of 2.27(0) Å as well as an angle of 141° between carbonyl groups of **Bal** and the Hf metal center of node, see Fig. S12†. Regarding the M-UiO-66-PDC/**Bal** systems, the orientation of the **Bal** molecules is such that the carbonyl groups face both the metal site (Hf or Zr) of the material and the N atoms of the PDC linker pyridine ring. The C−O···M interaction leads to intermolecular distances of 2.27 and 2.30 Å, with angles of 123° and 122° for Hf-UiO-66-PDC/**Bal** and Zr-UiO-66-PDC/**Bal**, respectively. As shown, the angles suffer a slight diminution in comparison to the BDC systems, which could be related to the presence of the N atom. Furthermore, the intermolecular contact between M-UiO-66-PDC and **Bal** between the N atom (N ··HOC-) of 3.55 and 3.52 Å, accompanied by C−H···N angles of 162° and 163° respectively, as displayed in the Fig. S13†.

View Article Online
DOI: 10.1039/D5DT00494B

In case of the **Ac** interacting with Lewis (metal center) and Brønsted (μ_3-O) acid sites, similar effects are observed for the carbonyl group. Specifically, in the monometallic-UiO-66 system, the final conformation consisted of two intermolecular interactions. The first is the interaction of the **Ac** carbonyl group shifted to a position closer to the metal center in the defective sites. The second interaction forms a hydrogen bond between a methyl group hydrogen atom and a μ3-O site O atom. The bimetallic-UiO-66 system shows the **Ac** final conformation comparable to the monometallic-UiO-66/**Ac** system. However, in contrast to the Zr/Hf-UiO-66-BDC/**Bal** system, the **Ac** carbonyl group interaction is produced with the Zr metallic center in the defective site (see Fig. S12b†) selected bond lengths for the monometallic-UiO-66/**Ac** systems are displayed in Fig. S14†. The estimated distance between the **Ac** carbonyl group and the materials metallic center, denoted as -C=O ⋯ M, is between 2.29 and 2.39 Å, see Fig. S14†. Additionally, the angle value ranges from 134 to 142°, as shown in Table S3, which is in concordance with those previously described interaction angles. The calculated -C-H⋯μ_3-O hydrogen bond length is between 2.00 and 2.30 Å see Figure S14. The [-C-H⋯μ_3-O] angle was in the range of 134 to 142° (see Table S3†).

To obtain a more comprehensive understanding of the intermolecular interactions between **Bal** and **Ac** molecules in the acid sites of the material, the energy decomposition analysis (EDA) and the natural orbital of chemical valence (NOCV) methods were calculated. The EDA results indicate that the electrostatic factor plays a significant role in stabilizing energy in all systems. For instance, in the M-UiO-66-PDC/**Bal** and M-UiO-66-PDC/**Ac** systems, the ΔE_{Elec} component accounts for approximately 55 to 58% of the overall stabilizing energy, as shown in Table S4. In the case of the M-UiO-66-BDC/**Bal** and M-UiO-66-BDC/Ac systems, about 45 to 50% of the overall stabilization is due to the ΔE_{Elec}. Besides, the calculations also indicated that orbital interactions play a significant role in the total stabilizing energy of all systems. It was observed that ΔE_{Orb} ranges from 33 to 42% for all systems. The ΔE_{Orb} refers to the stabilization energy resulting from the interaction of molecular orbitals between interacting species.

The results showed that **Bal** and **Ac** molecules might have a strong affinity for the acid sites (Lewis and Brønsted) present in the mono- and bimetallic UiO-66 studied structures. The ΔEO_{rb} component was examined using the NOCV method to investigate the intermolecular interactions.[42] [58]From NOCV deformation density channel ($\Delta\rho_i$) it was found that both molecules (*i.e.* **Bal** and **Ac**) interact with a metallic center. Equation 3 describes how the deformation density channels arising from NOCVs can be expressed as the movement of electron density out or into a specific

View Article Online
DOI: 10.1039/D5DT00494B

fragment. The plots of deformation density ($\Delta\rho_1$), shown in Figs. S15-S18†, indicate the flow of charge from the molecules (**Bal** or **Ac**, outflow) to the metal center (inflow) in all systems. In these NOCVs images the deformation density channels are represented by the reduction of electron density (outflow, red contours) and the accumulation of electron density (inflow, blue contours). Thus, in all systems, the main charge transfer channel $\Delta\rho_i$, evidence a charge flow from the carbonyl groups oxygen atoms lone pair of **Bal** or **Ac** to the MOFs metal center. On the other hand, energetic estimations, $\Delta E_{\mathbf{Orb}}(1)$, for each $\Delta\rho(1)$, account for 41 to 63% of the orbital component, see Table S3. No evidence was found regarding the interaction between the molecule (**Bal** or **Ac**) and the acid Brønsted sites of the material when examining the remaining significant deformation density channels, $\Delta\rho_{orb}(i)$, based on their corresponding energy, $\Delta E_{\mathbf{Orb}}$ (i). The analysis of all systems shows that the EDA-NOCV analysis uncovers the significance of Lewis sites in UiO-66's defective sites. These Lewis sites play a crucial role in the interactions between the adsorbate (**Bal** or **Ac**) and the adsorbent (UiO-66 material), which govern the adsorption mechanism of the **Bal**-**Ac** pair on the surface.

3.3 Catalytic activity

It has been described that the cross-aldol condensation between **Bal** and **Ac** produces C-C coupling. Therefore, acetone is deprotonated to form an enol or enolate-type nucleophile, and this generated intermediary molecule reacts with the carbonyl group of benzaldehyde (electrophile) to obtain a conjugated system of an α,β-unsaturated carbonyl as the final product. This reaction is interesting and important as it consists of two steps occurring in situ. First, α,β-hydroxyketone (B-ol) is formed according to the aldol reaction (see Fig. 2). Subsequently, a conjugated system of an α,β-unsaturated carbonyl corresponding to benzalacetone (see Figure 2, B-one) is obtained as the final product produced due to the dehydration of B-ol. Previous reports of layered double hydroxides show a large conversion (around 100%), whereas a low selectivity, which does not get over 55%[59,60]. Furthermore, the use of NaOH as homogeneous catalyst shows a large conversion and also a good conversion, however, the purification of the B-one is complicated[61]. A similar catalyst (as the herein report), constituted by the addition of Cs^+ over a β-zeolite has shown a conversion of 72% with a selectivity of 98%[62].

View Article Online
DOI: 10.1039/D5DT00494B

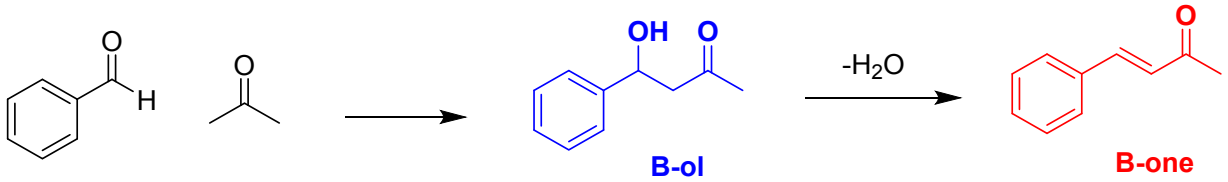

Fig. 2. Schematic reaction of cross-aldol condensation of benzaldehyde and acetone.

The catalytic and selective activity of the herein-studied MOFs in the cross-condensation of benzaldehyde and acetone to produce benzalacetone changed as the organic linker was altered. Figure 3a-c depicts the catalytic conversion development for mono- and bi-metallic UiO-66 catalysts with 1,4-benzenedicarboxylic acid (BDC) as an organic linker. While Fig. 3d-e shows the trend of catalytic activities based on cross-aldol condensation of benzaldehyde/acetone with 2,5-pyridindicarboxylic acid (PDC) as organic linkers. Also, this figure illustrates the differences in initial material conversion as a function of time for the five MOFs under study. Every catalyst increases the conversion over time, which might explain the variations of the acid-base characteristics in each material. Also, the absence of a linker (defect) creates Lewis's acid sites, like coordinatively unsaturated spots, that facilitate the reagent adsorption. However, according to the physicochemical analysis, all defective UiO-66 sites have a variety of acid sites that promote dynamic acidity throughout the condensation reaction. The production of enolate or enol intermediates during the aldol condensation depends on the presence of UiO-66 acid active sites. Furthermore, the presence of the free electron pair of nitrogen atoms in the MOFs organic linkers aromatic ring has a significant effect on each substance's acid-base characteristics. Similar to the previous results, some acetone auto-condensation reaction was observed when the bimetallic UiO-66 was used. However, the results obtained support the fact that the MOFs studied have a higher selectivity for the cross-coupling aldol condensation.

View Article Online
DOI: 10.1039/D5DT00494B

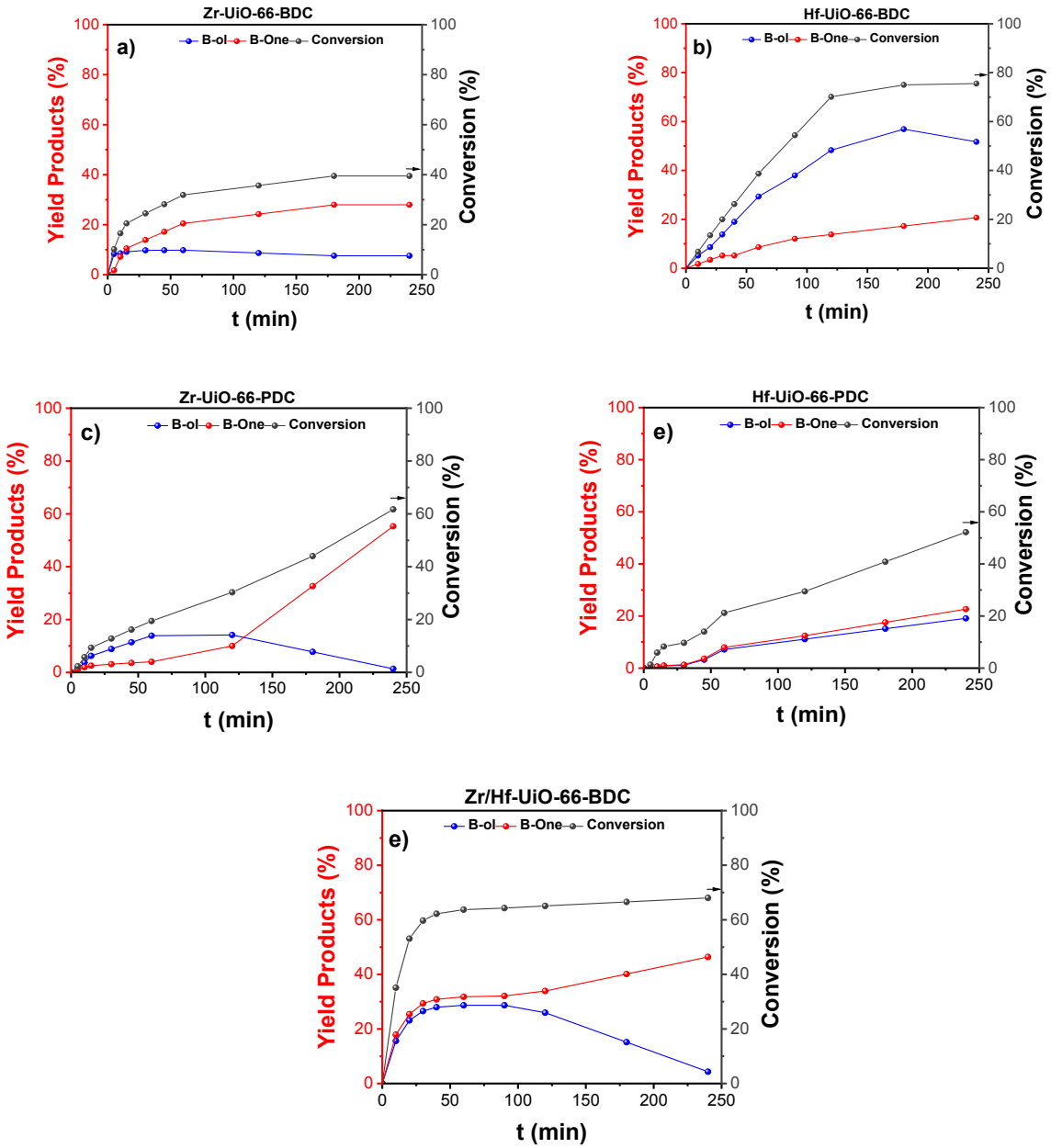

Fig. 3. Catalytic conversion over mono- and bimetallic UiO-66 via cross-coupling aldol condensation reaction.

In addition, Fig. 4 represents the MOFs' catalytic activity concerning the turnover frequency (TOF) behavior calculated from the initial reaction rate normalized by the total acidic sites for each material used. The more significant amount of MOFs acid sites might impact how benzaldehyde

View Article Online
DOI: 10.1039/D5DT00494B

interacts with the MOF and how it is adsorbed onto surfaces. However, the diversity of total acidic sites among the remaining 5 MOFs produces differences in catalytic activity, which suggests coordinated active site kinetics. As there is no specific kinetic route to create benzalacetone, this concerted mechanism connected to the concentration of acid-base sites reduces the initial reaction rate. [63] The catalytic environment of Zr/Hf-UiO-66 is more favorable for benzaldehyde conversion due to the formation of unique electronic and steric effects that influence the strength of the defect density in the MOF metal cluster. Concerning monometallic UiO-66, the interaction energy of the benzaldehyde on the material's surface is influenced by the oxophilic character of the metals in the SBU of MOFs, which leads to variations in the pace at which the target product forms. The higher the oxophilic character of the constituent metals of the SBU, the increase in the catalytic activity of the materials is expected. However, the presence of pyridinic groups in the organic ligand decreases the strength of the acidic sites in the metal clusters of MOFs, decreasing the catalytic activity toward C-C coupling formation.

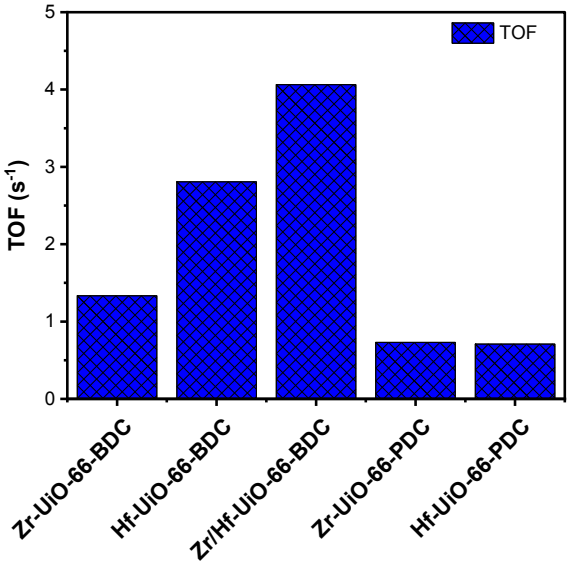

Fig. 4. Turnover-frequency as a function of total acid surface density UiO-66 catalysts for Cross-aldol condensation of benzaldehyde and acetone.

The relevance of active sites in the material vacancies is shown by a comparative examination of the interaction energies acquired using EDA-NOCV analysis, and the catalytic activity determined

View Article Online
DOI: 10.1039/D5DT00494B

using TOF. Specifically, the acidic sites play a key role in the interactions between the adsorbate (**Bal** or **Ac**) and the adsorbent (UiO-66 MOFs), influencing the **Bal-Ac** interaction process onto the surface. Fig. 5 depicts the trend of the total interaction energies of the **Bal-Ac** pair on the surface of each MOF vs the calculated TOF for this reaction. The TOF describes the quantity of molecules of benzaldehyde converted into the specified product per second. Because of the metal composition in the cluster, Zr/Hf-UiO-66 has the highest TOF due to the cooperative effects of total acidity, defectivity, site availability, and electronic distribution, which are impacted by the catalyst's acid site strength. In addition, this cooperative effect enhances the adsorption of the reactants (Bal-Ac) on the catalyst surface and consequently increases the possibility of the active site interactions with the reactants. Furthermore, the geometry optimization study reveals that Zr/Hf-UiO-66 has a distinct geometrical arrangement when interacting with **Bal** or **Ac**. Thus, the interacting system supports that **Bal** interacts preferentially with the Hf metal center at the defect site, whereas **Ac** interacts preferentially with Zr. Also, the main intermolecular interaction is given by a Hf···OHC- between the carbonyl groups of **Bal** and the Hf metal core of the node, as shown in Fig. S8a and S8b.†

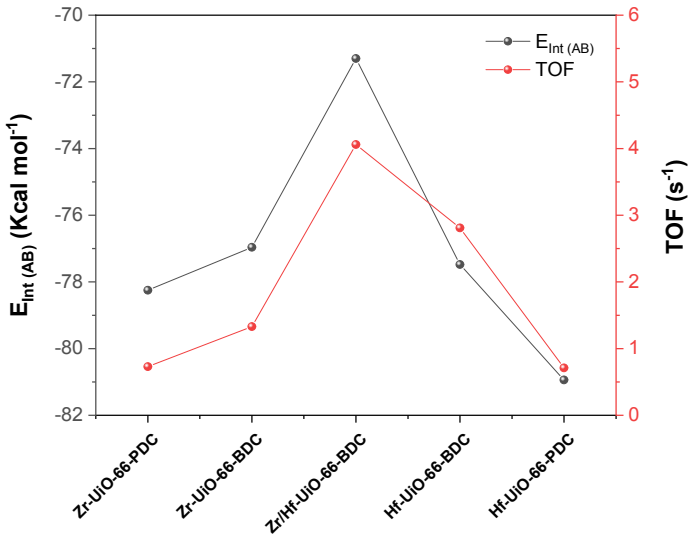

Fig. 5. Correlation between the turnover frequency and interaction energy for cross-aldol condensation (Bal/Ac) over MOFs.

View Article Online
DOI: 10.1039/D5DT00494B

Fig. 6 represents the selectivity behavior of all the MOFs under isoconversion conditions (30% of conversion), highlighting the variations in the β-hydroxyketone and benzalacetone concentrations. The differences in selectivity might be related to a modest variation in the active sites' nature of each catalyst and how these sites impact the intermolecular interaction geometry of the reactants on the catalyst's surface. As reported by Pazo et al.,[63] the water produced from aldol dehydration it adsorbs on the catalyst surface, changing the nature of the acid site. For this reason, UiO-66-BDC presents low selectivity towards the formation of the α,β-unsaturated. According to the results obtained, both UiO-66-PDCs are more selective for cross-aldol condensation than MOFs containing the BDC linker, because the electron pair of the PDC offers an influence on the nature of the active site of the material. While the hydrogen atom connected to the oxo atom of the μ_3-OH group protonates the acetone's carbonyl, the PDC nitrogen's electron pair is expected to interact with the carbonyl carbon of the benzaldehyde. This behavior suggests that, in addition to the free electron pair of the pyridine nitrogen, the acetone-benzaldehyde couple interacts primarily with three types of protons that are present in the UiO-66-PDC structure: μ_3 -OH, -OH_2, and -OH protons. The formation of hydrogen bonds and Van der Waals-type interactions cause these interactions, which are somewhat consistent with the previously reported theoretical computations.

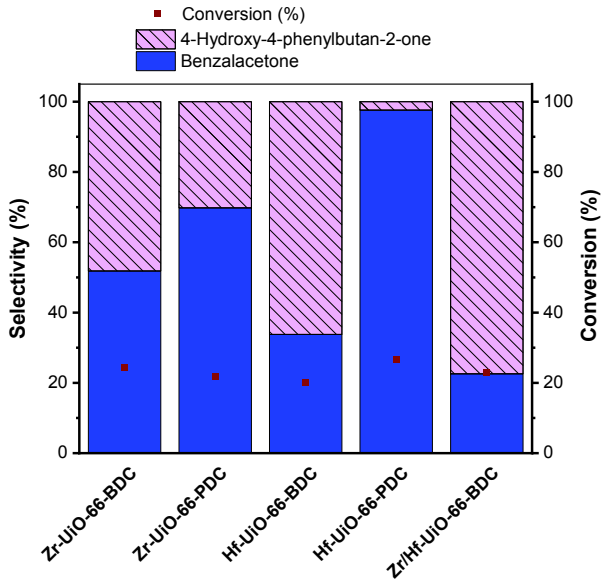

Fig. 6. Selectivity obtained at 20% conversion in UiO-66 catalysts.

View Article Online
DOI: 10.1039/D5DT00494B

Finally, a process of **Ac** enolization by the abstraction of the protons facilitated by the acid-base pairs in the frameworks is presented from thermal analyses of the acidity and basicity of each material. According to a proposal made by Rojas et al. [64,65], the metal center polarizes the acetone's carbonyl group. This polarization produces α-proton acidification, making its abstraction easier by the metal center's structural oxygen atom. The framework's bridging oxygen atom works as a base, creating an enolate. A combination of factors in Hf-UiO-66 has higher catalytic activity (Lewis's acidity, accessibility of active sites, pore volume, and surface contacts). A distinct behavior is observed when the pyridine groups are in the MOF's organic linker. Thus, the adsorption modes of the reagents on the active sites, as depicted in Fig. 7, indicate that the aldol condensation on UiO-66 with BDC and PDC exhibits different kinetic mechanisms depending on the metal and organic linker present in the MOFs structure.

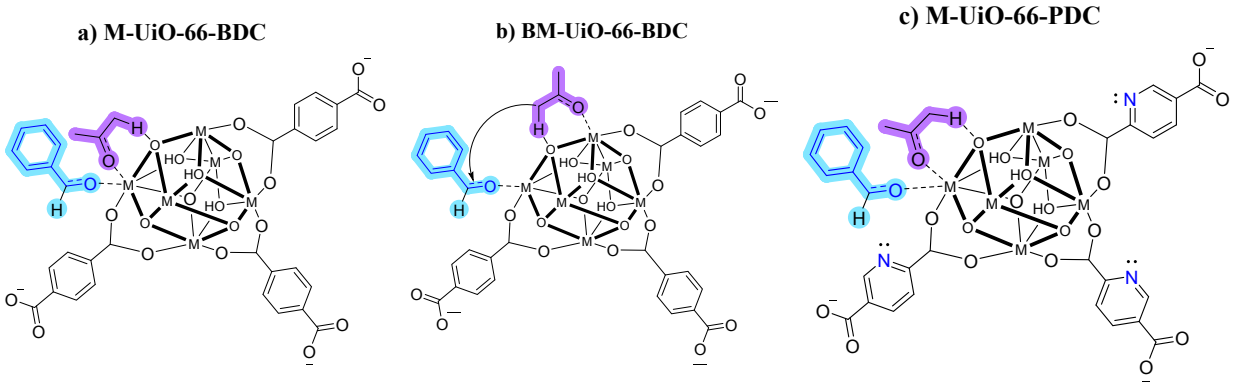

Fig. 7. Proposal of an adsorption mechanism of the benzaldehyde-acetone pair on the surface of a) M-UiO-66-BDC, b) Zr/Hf-UiO-66-BDC, and c) M-UiO-66-PDC.

Kinetic modeling for UiO-66

The aldol condensation of benzaldehyde with acetone is generally acknowledged to be caused by the presence of a catalyst with acidic or basic properties.[11,65,66] Different possible reaction mechanisms were studied to understand further the cross-coupling condensation mechanism using UiO-66 as a catalyst. Thus, the UiO-66 catalytic reaction to generate benzalacetone involves six stages, according to the proposed reaction mechanism (Fig. 8a). This mechanism relies on the UiO-66 material's ability to possess catalytically active sites, which have been proposed to be generated

View Article Online
DOI: 10.1039/D5DT00494B

during the synthesis of the material[54]. Specifically, the Lewis acid sites are generated due to the MOF's defect creation, resulting in coordinatively unsaturated sites.

The steps of the cross-aldol reaction depicted in Fig. 8a will be first discussed. According to the suggested Langmuir-Hinshelwood mechanism (LHM), both reagents are adsorbed through their carbonyl oxygen group on adjacent MOF metallic atoms (steps 1-2). The **Ac** molecule is activated by the α-carbon atom, inducing a hydrogen transfer to the metal cluster μ_3-oxygen. An enolate intermediate [67] is created in the process, which is stabilized due to the contact with the metal active site (step 2). Metal-bonded enolate has a high tendency to attack the adsorbed benzaldehyde. Afterwards, a new intermediary state is created after a nucleophilic attack at step 3 (producing the C-C coupling). This step involves the breakage of the enolate linked to the metal. The C-C coupling product generates a more stable intermediate along the reaction pathway in step 3. The hydrogen attached to the μ_3-oxygen atom in step 3 protonates the C-C coupling product, creating the aldol product. The molecule is rearranged into the active site of the MOF, and the α-carbon atom is deprotonated. Then, the α-carbon atom protonates the metal cluster μ_3-oxygen atom (step 5). Then, the hydroxyl group is broken from the obtained intermediary, forming the primary product, benzalacetone (step 6). Based on the calculated kinetic constants, the product is released quickly. Subsequently, water is created during the aldol condensation processes while benzalacetone is kept in the reaction medium. Fig. 8b shows the adsorption of **Bal** and **Ac** on two active sites of different natures. Due to the oxophilic difference of the clusters' metals, the less acidic reagent (Ac) likely adsorbs on more oxophilic metal (Hf) and vice versa, as suggested by theoretical calculations. According to the above, bimolecular surface reaction mechanisms are proposed at one site when the MOF cluster is monometallic and at two sites when it is bimetallic.

View Article Online
DOI: 10.1039/D5DT00494B

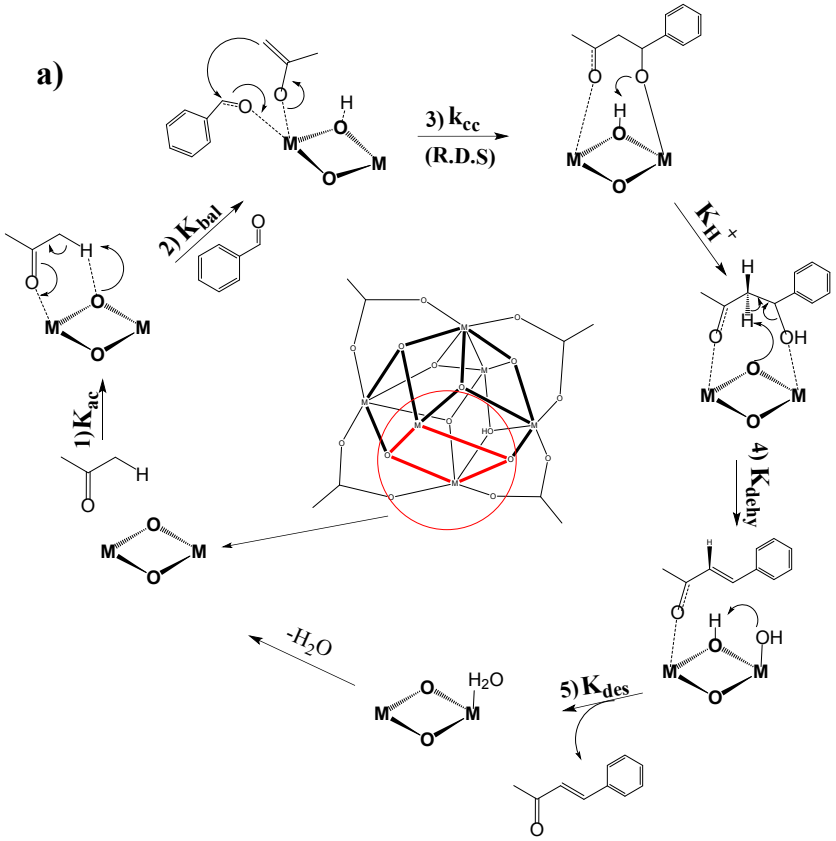

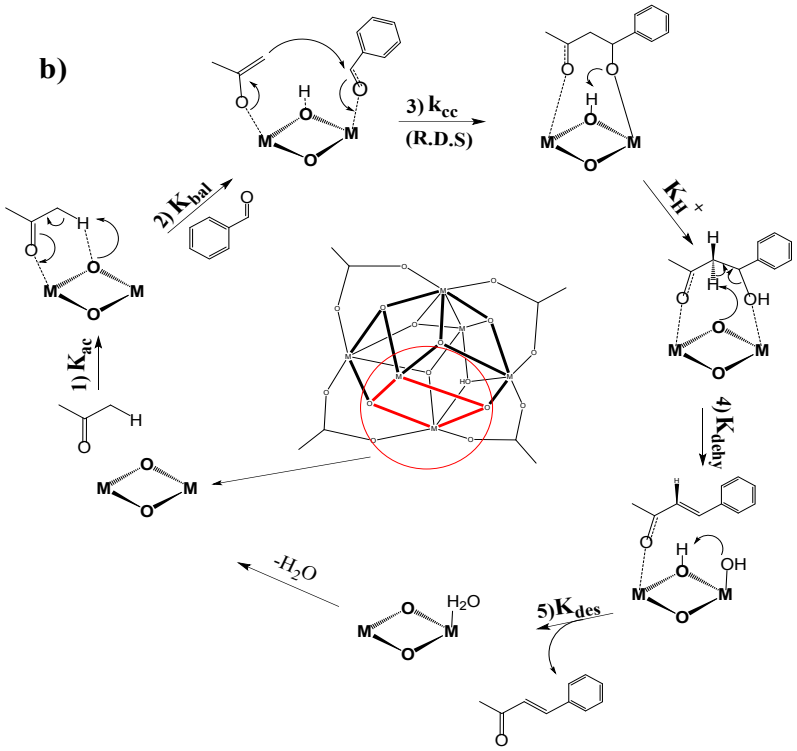

View Article Online
DOI: 10.1039/D5DT00494B

Fig. 8. Proposal of the surface reaction mechanism of UiO-66-BDC catalysts using the Langmuir-Hinshelwood model a) bimolecular one site b) bimolecular two sites.

It has been observed in the kinetic study that the determining step of the reaction is mainly associated with the subsequent protonation/deprotonation of the reactive molecules. The hydroxyl group is then dehydroxylated by chemisorption at the metal Lewis acid site. According to Pazo et al., a modification to the catalytic site composition is suggested.[63] Accordingly, the elementary steps for benzaldehyde conversion can be described by the one-site L-H mechanism with the following equations, where "*" represents an active site, **Bol** is the reaction intermediary (beta hydroxy ketone), and **Bone** is the reaction product (benzalacetone).

$$\mathrm{Bal} + * \overset{K_{Bal}}{\rightleftharpoons} Bal - * \quad (1)$$

$$\mathrm{Ac} + * \overset{K_{Ac}}{\rightleftharpoons} Ac - * \quad (2)$$

$$Bal - * + Ac - * \overset{k_{cc}}{\rightarrow} Bol + 2 * \ (rds) \quad (3)$$

$$Bol + * \overset{K_{Bol}}{\rightleftharpoons} B - * \quad (4)$$

$$Bol - * \overset{K_{dehy}}{\rightleftharpoons} Bone - * + H_2O \quad (5)$$

$$Bone - * \overset{K_{des}}{\rightleftharpoons} Bone + * \quad (6)$$

For the two sites, the L-H mechanism reaction steps involve the following equations:

$$\mathrm{Bal} + *_1 \overset{K_{Bal}}{\rightleftharpoons} Bal - *_1 \quad (7)$$

$$\mathrm{Ac} + *_2 \overset{K_{Ac}}{\rightleftharpoons} Ac - *_2 \quad (8)$$

$$Bal - *_1 + Ac - *_2 \overset{k_{cc}}{\rightarrow} Bol - *_1 + *_2 \ (rds) \quad (9)$$

$$Bol - *_1 \overset{K_{dehy}}{\rightleftharpoons} Bone - *_2 + H_2O \quad (10)$$

$$Bone - *_2 \overset{K_{des}}{\rightleftharpoons} Bone + *_2 \quad (11)$$

Under the reaction conditions, for the one-site and dual-site L-H mechanism, the rate-determining step (RDS) is the surface reaction (equation 3). This step corresponds to the acetone and benzaldehyde adsorbed reaction to produce b-hydroxy ketone (equation 3), as the presence of **Bol**

View Article Online
DOI: 10.1039/D5DT00494B

was revealed by gas chromatography. With these considerations, the rate expressions correspond to equation 7 for one-site L-H and equation 8 for a dual-site equation.

$$r = k_{cc}K_{Bal}K_{Ac}[Bal][Ac]\theta_v^2 \quad \text{(Eq. 7)}$$

$$r = k_{cc}K_{Bal}K_{Ac}[Bal][Ac]\theta_{v_1}\theta_{v_2} \quad \text{(Eq. 8)}$$

Where θ represents the fraction of surface area covered by each compound in the reaction, the mathematical clearance of this model leads to the rate expression for the L-H (more details for both models can be found in supplementary material):

$$r = \frac{k_{cc}K_{Bal}K_{Ac}[Bal][Ac]}{\left(1+K_{bal}[Bal]+K_{Ac}[Ac]+K_{Bol}[Bol]+\frac{[Bone]}{K_{des}}\right)^2} \quad \text{(Eq. 9)}$$

Then,

$$\theta_v = \frac{1}{\left(1+K_{bal}[Bal]+K_{Ac}[Ac]+K_{Bol}[Bol]+\frac{[Bone]}{K_{des}}\right)}$$

(Eq. 10)

Simplifying the equation, it follows that,

$$r = \frac{k'[Bal][Ac]}{\left(1+K_{bal}[Bal]+K_{Ac}[Ac]+K_{Bol}[Bol]+\frac{[Bone]}{K_{des}}\right)^2} \quad \text{(Eq. 11)}$$

$$r = \frac{k'[Bal][Ac]}{(1+K_{bal}[Bal]+K_{Ac}[Ac])^2} \quad \text{(Eq. 12)}$$

While for the two-site L-H model, the rate equation becomes:

$$r = \frac{k_{cc}K_{Bal}K_{Ac}[Bal][Ac]L_1L_2}{(1+K_{Ac}[Ac]+\frac{[Bone]}{K_{dehy}K_{des}}+\frac{[Bone]}{K_{des}})(1+K_{bal}[Bal])} \quad \text{(Eq. 13)}$$

and

$$\theta_{v_1}\theta_{v_2} = \frac{L_1L_2}{(1+K_{Ac}[Ac]+\frac{[Bone]}{K_{dehy}K_{des}}+\frac{[Bone]}{K_{des}})(1+K_{bal}[Bal])} \quad \text{(Eq. 14)}$$

Simplifying the equation, it is finally obtained that,

View Article Online
DOI: 10.1039/D5DT00494B

$$r = \frac{k''[Bal][Ac]}{(1+K_{Ac}[Ac]+\frac{[Bone]}{K_{dehy}K_{des}}+\frac{[Bone]}{K_{des}})(1+K_{bal}[Bal])} \quad \text{(Eq. 15)}$$

$$r = \frac{k''[Bal][Ac]}{(1+K_{Ac}[Ac])(1+K_{bal}[Bal])} \quad \text{(Eq. 16)}$$

The results of adjustment of the kinetic models with experimental data are shown in Fig. S19. † As it is possible to appreciate, the one-site L-H model best fits the experimental data, with an RSS value of >0.9976 when the UiO-66 is monometallic with BDC as a linker and >0.9885 with PDC as an organic linker. The RSS value of the two-site L-H model is 0.9965 for the Zr/Hf- UiO-66. This strongly suggests that the reaction is carried out by adsorbing **Bal** and **Ac,** as shown in Figure 8a for the monometallic BDC MOFs. Both adsorbed react by nucleophilic attack of the enolate towards the benzaldehyde to generate **B-ol**. Finally, Table 3 shows the results of the kinetic parameters obtained by the bimolecular one-site L-H model. From the adsorption constant data, it is possible to establish that **Bal** and **Ac** has a greater affinity with the surface than the other compounds similar to that observed by DFT. This possibly explains why its generation was not observed during experimental analyses. Also, the adsorption constant for **Bone** is lower compared to the adsorption constant for the rest of the analyzed compounds, which favors the desorption of the product once **Bol** has been dehydrated on the surface of the catalyst. Moreover, in the bimolecular dual-site model, the rate limiting step is the attack of the enolate species by another **Ac** acting as electrophile and adsorbed at a vicinal Lewis acid site, which facilitates the C–C coupling.

Table 3. Optimized kinetic parameters obtained by fitting benzaldehyde and acetone condensation data on MOFs catalysts with bimolecular Langmuir-Hinshelwood models.

	Rate Constant	**Adsorption Equilibrium constant**			
	(mmol g^{-1} s^{-1})	**(mmol^{-1})**			
MOFs	**k_{cc}**	**$K_{1(bal)}$**	**$K_{2(ac)}$**	**RSS**	**Model**
Zr-UiO-66-BDC	1.059	0.1342	0.0089	0.9994	OSLH
Zr/Hf-UiO-66-BDC	19.638	0.0007	0.0303	0.9965	TSLH
Hf-UiO-66 -BDC	3.809	0.0211	0.0915	0.9976	OSLH
Zr-UiO-66-PDC	3.669	0.0016	0.0034	0.9885	OSLH
Hf-UiO-66-PDC	4.926	0.0044	0.0219	0.9978	OSLH

View Article Online
DOI: 10.1039/D5DT00494B

OSLH: one site Langmuir-Hinshelwood model, TSLH: Two site Langmuir-Hinshelwood model

The same reaction mechanism was examined for the cross-aldol condensation found for the UiO-66-PDC, which shows the importance of the oxo-atom presence in the inorganic piece as the base site. Fig. 9 shows the proposed deprotonation of the acetone following adsorption on the Lewis acid site of the metal cluster in order to form the enolate by proton transfer from the α-carbon to the μ_3-oxygen. The pyridine group of the organic linker functions as an electron donor of the linker and does not actively participate in the reaction, and the effects of its presence on the various steps of the reaction profile appear to be minor. The linker's nature alters the reaction's kinetics due to replacing the phenyl group with the pyridine group, strengthening the benzaldehyde's contact, and forming a pseudo-hydrogen bridge connection. This contrasts with the findings of Hajek, et al.[12], who reported that using UiO-66 functionalized with an amino group resulted in slightly higher activity for cross-aldol formation due to slightly stronger adsorption. In summary, the adsorption of the reactants, combined with a slightly lower barrier for the pyridine-functionalized material, would point toward a lower catalytic activity.

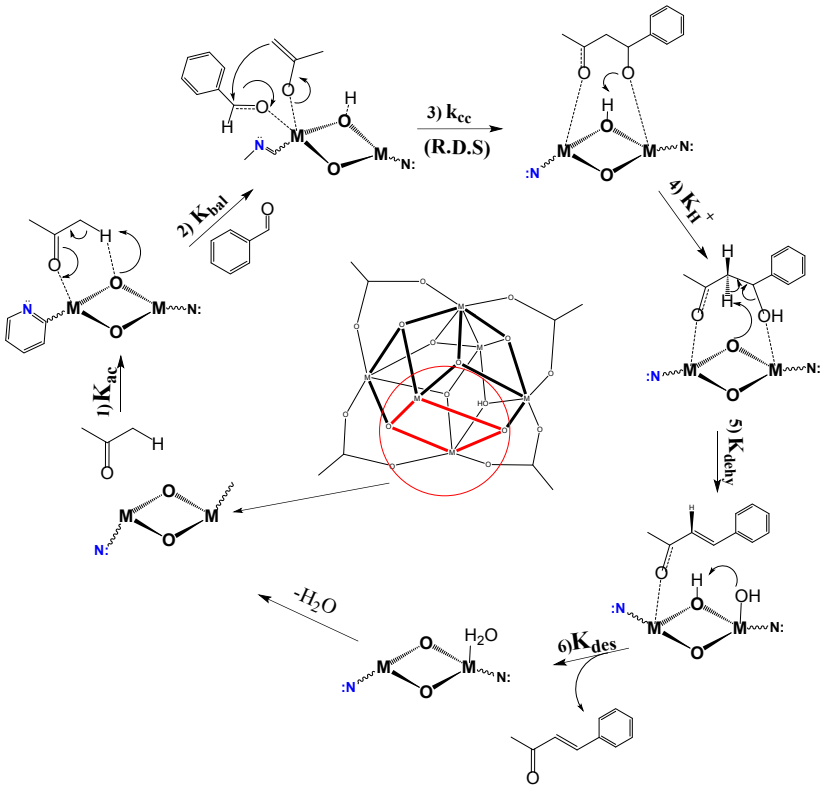

View Article Online
DOI: 10.1039/D5DT00494B

Fig. 9. Proposal of the surface reaction mechanism of UiO-66-PDC using the Langmuir-Hinshelwood model.

Lastly, it has been noted that this catalytic process involves several variables, including acidic/basic sites, acid strength, pore volume, surface contacts, and active site accessibility that affect the kinetics of the reaction. It should be noted that the enhanced abilities of all MOFs to condensate acetone with benzaldehyde and dehydrate the aldol intermediate to form the α,β-unsaturated exhibit desirable properties to be used in aldol condensation. Furthermore, Figure S20 illustrates the Zr/Hf-UiO-66 catalyst's stability in relation to the production of benzalacetone. After the fifth repetition, the Zr/Hf-UiO-66 catalyst progressively loses its catalytic yield by around 17%, according to the shown results. In order to give an explanation to the loss in activity, XRD, surface area, FT-IR, TGA and XPS experiments were performed over the used catalyst. In Figures S21-25 can be found the obtained results. Textural and crystallography changes can be observed, which could support the collapse of some portions of the MOF. However, the microporosity and thermal stability are maintained. As can be observed in the XPS analysis, a slight composition was observed on the surface of the material, which also support some collapse of the MOF.

4 Conclusions

All the synthesized MOFs presented textural, crystalline, and acid-base characteristics according to the UiO-66 type materials. These MOFs were used in the catalytic experiments performed in this work. A higher initial catalytic activity was observed for the cross-aldol product, and benzaldehyde had a higher initial reaction rate with the MOF. Using Zr-UiO-66-BDC, Hf-UiO-66-BDC, and Zr/Hf-UiO-66-BDC, the reaction kinetics data were verified and compared with their corresponding UiO-66-PDC with Zr and Hf. However, the experiments predict a similar performance of both catalysts after four reaction hours. The total acid sites play a crucial role in the interactions between the adsorbate (**Bal** or **Ac**) and the adsorbent (UiO-66 materials), which influence the Bal-Ac adsorption process on the surface. There is an observed trend between the DFT total interaction energies of the **Bal** and **Ac** pair on the surface of each MOF vs. the TOF. In all the catalysts, the experiment clearly shows a high selectivity towards the cross-product; however, in the parent UiO-66, there is competition with the self-aldol condensation in the very early phases of the reaction. The availability of active metal sites may also influence the activity

View Article Online
DOI: 10.1039/D5DT00494B

ratio change of UiO-66 vs UiO-66-PDC as a function of reaction time, although this needs more sophisticated approaches. Finally, the bimetallic UiO-66 presented a bimolecular kinetic adjustment of the two-site L-H model. In addition, as it is possible to appreciate, the one-site L-H model best fits the experimental data, with an RSS value of >0.9976 when the UiO-66 is monometallic with BDC as a linker and >0.9885 with PDC as an organic linker.

Acknowledgements

This work was supported by ANID-Chile under FONDECYT-Chile project 1241917, 1220763, PIA CCTEAFB170007, and FONDEQUIP EQM 160070. This work was also supported by Fondap/serc chile/1523A0006. The authors thank the financial support given by the European Commission through the H2020-MSCA-RISE-2020 BIOALL project (Grant Agreement: 101008058),

References

(1) Butova, V. V; Soldatov, M. A.; Guda, A. A.; Lomachenko, K. A.; Lamberti, C. Metal-Organic Frameworks: Structure, Properties, Methods of Synthesis and Characterization. *Russian Chemical Reviews* **2016**, *85* (3), 280–307. https://doi.org/10.1070/RCR4554.

(2) Herbst, A.; Janiak, C. MOF Catalysts in Biomass Upgrading towards Value-Added Fine Chemicals. *CrystEngComm* **2017**, *19* (29), 4092–4117. https://doi.org/10.1039/c6ce01782g.

(3) Yang, D.; Gates, B. C. Catalysis by Metal Organic Frameworks: Perspective and Suggestions for Future Research. *ACS Catal* **2019**, *9* (3), 1779–1798. https://doi.org/10.1021/acscatal.8b04515.

(4) García-García, P.; Moreno, J. M.; Díaz, U.; Bruix, M.; Corma, A. Organic-Inorganic Supramolecular Solid Catalyst Boosts Organic Reactions in Water. *Nature communications*. Instituto de Tecnología Química, UPV-CSIC, Universidad Politécnica de Valencia, Avenida de los Naranjos s/n, E-46022 Valencia, Spain. 2016, p 10835. https://doi.org/10.1038/ncomms10835.

(5) Rechac, V. L.; Cirujano, F. G.; Corma, A.; Llabrés i Xamena, F. X. Diastereoselective Synthesis of Pyranoquinolines on Zirconium-Containing UiO-66 Metal-Organic Frameworks. *Eur J Inorg Chem* **2016**, *2016* (27), 4512–4516. https://doi.org/10.1002/EJIC.201600372.

(6) Yabushita, M.; Li, P.; Islamoglu, T.; Kobayashi, H.; Fukuoka, A.; Farha, O. K.; Katz, A. Selective Metal-Organic Framework Catalysis of Glucose to 5-Hydroxymethylfurfural Using Phosphate-

View Article Online
DOI: 10.1039/D5DT00494B

Modified NU-1000. *Ind Eng Chem Res* **2017**, *56* (25), 7141–7148. https://doi.org/10.1021/ACS.IECR.7B01164/SUPPL_FILE/IE7B01164_SI_001.PDF.

(7) Dhakshinamoorthy, A.; Opanasenko, M.; Čejka, J.; Garcia, H. Metal Organic Frameworks as Heterogeneous Catalysts for the Production of Fine Chemicals. *Catal Sci Technol* **2013**, *3* (10), 2509–2540. https://doi.org/10.1039/C3CY00350G.

(8) Cavka, J. H.; Jakobsen, S.; Olsbye, U.; Guillou, N.; Lamberti, C.; Bordiga, S.; Lillerud, K. P. A New Zirconium Inorganic Building Brick Forming Metal Organic Frameworks with Exceptional Stability. *J. Am. Chem. Soc.* **2008**, *130* (42), 13850–13851. https://doi.org/10.1021/ja8057953.

(9) Wu, H.; Yildirim, T.; Zhou, W. Exceptional Mechanical Stability of Highly Porous Zirconium Metal-Organic Framework UiO-66 and Its Important Implications. *Journal of Physical Chemistry Letters* **2013**, *4* (6), 925–930. https://doi.org/10.1021/JZ4002345/SUPPL_FILE/JZ4002345_SI_006.CIF.

(10) Rimoldi, M.; Howarth, A. J.; Destefano, M. R.; Lin, L.; Goswami, S.; Li, P.; Hupp, J. T.; Farha, O. K. Catalytic Zirconium/Hafnium-Based Metal-Organic Frameworks. *ACS Catal* **2017**, *7* (2), 997–1014. https://doi.org/10.1021/ACSCATAL.6B02923/ASSET/IMAGES/MEDIUM/CS-2016-02923U_0014.GIF.

(11) Vermoortele, F.; Ameloot, R.; Vimont, A. An Amino-Modified Zr-Terephthalate Metal – Organic Framework as an Acid – Base Catalyst for Cross-Aldol Condensation w. **2011**, 1521–1523. https://doi.org/10.1039/c0cc03038d.

(12) Hajek, J.; Vandichel, M.; Van De Voorde, B.; Bueken, B.; De Vos, D.; Waroquier, M.; Van Speybroeck, V. Mechanistic Studies of Aldol Condensations in UiO-66 and UiO-66-NH2 Metal Organic Frameworks. *J Catal* **2015**, *331*, 1–12. https://doi.org/10.1016/j.jcat.2015.08.015.

(13) Yang, Q.; Wiersum, A. D.; Llewellyn, P. L.; Guillerm, V.; Serre, C.; Maurin, G. Functionalizing Porous Zirconium Terephthalate UiO-66(Zr) for Natural Gas Upgrading: A Computational Exploration. *Chemical Communications* **2011**, *47* (34), 9603–9605. https://doi.org/10.1039/C1CC13543K.

(14) Kandiah, M.; Usseglio, S.; Svelle, S.; Olsbye, U.; Lillerud, K. P.; Tilset, M. Post-Synthetic Modification of the Metal–Organic Framework Compound UiO-66. *J Mater Chem* **2010**, *20* (44), 9848–9851. https://doi.org/10.1039/C0JM02416C.

View Article Online
DOI: 10.1039/D5DT00494B

(15) Cadiau, A.; Lee, J. S.; Damasceno Borges, D.; Fabry, P.; Devic, T.; Wharmby, M. T.; Martineau, C.; Foucher, D.; Taulelle, F.; Jun, C.-H.; Hwang, Y. K.; Stock, N.; De Lange, M. F.; Kapteijn, F.; Gascon, J.; Maurin, G.; Chang, J.-S.; Serre, C. Design of Hydrophilic Metal Organic Framework Water Adsorbents for Heat Reallocation. *Advanced Materials* **2015**, *27* (32), 4775–4780. https://doi.org/https://doi.org/10.1002/adma.201502418.

(16) Lescouet, T.; Chizallet, C.; Farrusseng, D. The Origin of the Activity of Amine-Functionalized Metal–Organic Frameworks in the Catalytic Synthesis of Cyclic Carbonates from Epoxide and CO2. *ChemCatChem* **2012**, *4* (11), 1725–1728. https://doi.org/10.1002/CCTC.201200288.

(17) Panchenko, V. N.; Matrosova, M. M.; Jeon, J.; Won Jun, J.; Timofeeva, M. N.; Jhung, S. H. Catalytic Behavior of Metal-Organic Frameworks in the Knoevenagel Condensation Reaction. **2014**. https://doi.org/10.1016/j.jcat.2014.05.018.

(18) Dhakshinamoorthy, A.; Opanasenko, M.; Čejka, J.; Garcia, H. Metal Organic Frameworks as Solid Catalysts in Condensation Reactions of Carbonyl Groups. *Adv Synth Catal* **2013**, *355* (2–3), 247–268. https://doi.org/10.1002/adsc.201200618.

(19) Li, D.; Shi, F.; Peng, J.; Guo, S.; Deng, Y. Application of Functional Ionic Liquids Possessing Two Adjacent Acid Sites for Acetalization of Aldehydes. *J Org Chem* **2004**, *69* (10), 3582–3585. https://doi.org/10.1021/jo034859l.

(20) Baio Ferreira, G. K.; Carvalho, C.; Nakagaki, S. Studies of the Catalytic Activity of Iron (III) Porphyrins for the Protection of Carbonyl Groups in Homogeneous Media. *CATALYSTS* **2019**, *9* (4). https://doi.org/10.3390/catal9040334.

(21) Antunes, M. M.; Amarante, T. R.; Valente, A. A.; Almeida Paz, F. A.; Goncalves, I. S.; Pillinger, M. A Linear Trinuclear Oxidodiperoxido-Molybdenum(VI) Complex with Single Triazole Bridges: Catalytic Activity in Epoxidation, Alcoholysis, and Acetalization Reactions. *ChemCatChem* **2018**, *10* (13, SI), 2782–2791. https://doi.org/10.1002/cctc.201800232.

(22) Pinheiro, A. L. G.; do Carmo, J. V. C.; Carvalho, D. C.; Oliveira, A. C.; Rodríguez-Castellón, E.; Tehuacanero-Cuapa, S.; Otubo, L.; Lang, R. Bio-Additive Fuels from Glycerol Acetalization over Metals-Containing Vanadium Oxide Nanotubes (MeVOx-NT in Which, Me = Ni, Co, or Pt). *Fuel Processing Technology* **2019**, *184*, 45–56. https://doi.org/https://doi.org/10.1016/j.fuproc.2018.11.008.

View Article Online
DOI: 10.1039/D5DT00494B

(23) Hosseini, M.-S.; Masteri-Farahani, M. Surface Functionalization of Magnetite Nanoparticles with Sulfonic Acid and Heteropoly Acid: Efficient Magnetically Recoverable Solid Acid Catalysts. *CHEMISTRY-AN ASIAN JOURNAL* **2019**, *14* (7), 1076–1083. https://doi.org/10.1002/asia.201801810.

(24) Arrozi, U. S. F.; Wijaya, H. W.; Patah, A.; Permana, Y. Efficient Acetalization of Benzaldehydes Using UiO-66 and UiO-67: Substrates Accessibility or Lewis Acidity of Zirconium. *Appl Catal A Gen* **2015**, *506*, 77–84. https://doi.org/10.1016/j.apcata.2015.08.028.

(25) Wang, P.; Feng, J.; Zhao, Y.; Wang, S.; Liu, J. MOF-Derived Tungstated Zirconia as Strong Solid Acids toward High Catalytic Performance for Acetalization. *ACS Appl Mater Interfaces* **2016**, *8* (36), 23755–23762. https://doi.org/10.1021/acsami.6b08057.

(26) Mortazavi, S.-S.; Abbasi, A.; Masteri-Farahani, M.; Farzaneh, F. Sulfonic Acid Functionalized MIL-101(Cr) Metal-Organic Framework for Catalytic Production of Acetals. *ChemistrySelect* **2019**, *4* (25), 7495–7501. https://doi.org/10.1002/slct.201901070.

(27) Hinshelwood, C. N. The Kinetics of Chemical Change in Gaseous Systems. *Nature* **1927**, *119* (3004), 771–773. https://doi.org/10.1038/119771a0.

(28) Katz, M. J.; Brown, Z. J.; Colón, Y. J.; Siu, P. W.; Scheidt, K. A.; Snurr, R. Q.; Hupp, J. T.; Farha, O. K. A Facile Synthesis of UiO-66, UiO-67 and Their Derivatives. *Chemical Communications* **2013**, *49* (82), 9449–9451. https://doi.org/10.1039/c3cc46105j.

(29) Waitschat, S.; Fröhlich, D.; Reinsch, H.; Terraschke, H.; Lomachenko, K. A.; Lamberti, C.; Kummer, H.; Helling, T.; Baumgartner, M.; Henninger, S.; Stock, N. Synthesis of M-UiO-66 (M = Zr, Ce or Hf) Employing 2,5-Pyridinedicarboxylic Acid as a Linker: Defect Chemistry, Framework Hydrophilisation and Sorption Properties. *Dalton Transactions* **2018**, *47* (4), 1062–1070. https://doi.org/10.1039/c7dt03641h.

(30) Mancuso, J. L.; Mroz, A. M.; Le, K. N.; Hendon, C. H. Electronic Structure Modeling of Metal-Organic Frameworks. *Chem Rev* **2020**, *120* (16), 8641–8715. https://doi.org/10.1021/acs.chemrev.0c00148.

(31) Pazo-Carballo, C.; Blanco, E.; Camu, E.; Leiva, A.; Hidalgo-Rosa, Y.; Zarate, X.; Dongil, A. B.; Schott, E.; Escalona, N. Theoretical and Experimental Study for Cross-Coupling Aldol Condensation over

View Article Online
DOI: 10.1039/D5DT00494B

Mono- and Bimetallic UiO-66 Nanocatalysts. *ACS Appl Nano Mater* **2023**, *6* (7), 5422–5433. https://doi.org/10.1021/acsanm.2c05555.

(32) te Velde, G.; Bickelhaupt, F. M.; Baerends, E. J.; Fonseca Guerra, C.; van Gisbergen, S. J. A.; Snijders, J. G.; Ziegler, T. Chemistry with ADF. *J. Comput. Chem.* **2001**, *22* (9), 931–967. https://doi.org/10.1002/jcc.1056.

(33) Atanasov, M.; Aravena, D.; Suturina, E.; Bill, E.; Maganas, D.; Neese, F. First Principles Approach to the Electronic Structure, Magnetic Anisotropy and Spin Relaxation in Mononuclear 3d-Transition Metal Single Molecule Magnets. *Coord Chem Rev* **2015**, *289–290* (1), 177–214. https://doi.org/10.1016/j.ccr.2014.10.015.

(34) Lenthe, E. Van; Baerends, E. J.; Snijders, J. G.; Lenthe, E. Van; Baerends, E. J.; Snijders, J. G. Relativistic Regular Twocomponent Hamiltonians Relativistic Regular Two-Component Hamiltonians. *J Chem Phys* **1993**, *99.6*, 4597–4610. https://doi.org/10.1063/1.466059.

(35) Zhao, Y.; Truhlar, D. G. A New Local Density Functional for Main-Group Thermochemistry, Transition Metal Bonding, Thermochemical Kinetics, and Noncovalent Interactions. *Journal of Chemical Physics* **2006**, *125* (19). https://doi.org/10.1063/1.2370993.

(36) Van Lenthe, E.; Baerends, E. J. Optimized Slater-Type Basis Sets for the Elements 1-118. *J Comput Chem* **2003**, *24* (9), 1142–1156. https://doi.org/10.1002/jcc.10255.

(37) Tao, J.; Perdew, J. P.; Staroverov, V. N.; Scuseria, G. E. Climbing the Density Functional Ladder: Nonempirical Meta–Generalized Gradient Approximation Designed for Molecules and Solids. *Phys Rev Lett* **2003**, *91* (14), 3–6. https://doi.org/10.1103/PhysRevLett.91.146401.

(38) Sagan, F.; Mitoraj, M. P. Kinetic and Potential Energy Contributions to a Chemical Bond from the Charge and Energy Decomposition Scheme of Extended Transition State Natural Orbitals for Chemical Valence. *Journal of Physical Chemistry A* **2019**, *123* (21), 4616–4622. https://doi.org/10.1021/acs.jpca.9b01420.

(39) Mitoraj, M. P.; Michalak, A.; Ziegler, T. A Combined Charge and Energy Decomposition Scheme for Bond Analysis. *J Chem Theory Comput* **2009**, *5* (4), 962–975. https://doi.org/10.1021/ct800503d.

View Article Online
DOI: 10.1039/D5DT00494B

(40) Grimme, S.; Antony, J.; Ehrlich, S.; Krieg, H. A Consistent and Accurate Ab Initio Parametrization of Density Functional Dispersion Correction (DFT-D) for the 94 Elements H-Pu. *Journal of Chemical Physics* **2010**, *132* (15), 5585. https://doi.org/10.1063/1.3382344.

(41) Grimme, S. Density Functional Theory with London Dispersion Corrections. *Wiley Interdiscip Rev Comput Mol Sci* **2011**, *1* (2), 211–228. https://doi.org/10.1002/wcms.30.

(42) Mitoraj, M. P. Bonding in Ammonia Borane: An Analysis Based on the Natural Orbitals for Chemical Valence and the Extended Transition State Method (ETS-NOCV). *Journal of Physical Chemistry A* **2011**, *115* (51), 14708–14716. https://doi.org/10.1021/jp209712s.

(43) Mitoraj, M. P.; Michalak, A.; Ziegler, T. On the Nature of the Agostic Bond between Metal Centers and ??-Hydrogen Atoms in Alkyl Complexes. An Analysis Based on the Extended Transition State Method and the Natural Orbitals for Chemical Valence Scheme (ETS-NOCV). *Organometallics* **2009**, *28* (13), 3727–3733. https://doi.org/10.1021/om900203m.

(44) Devi, K.; Gorantla, S. M. N. V. T.; Mondal, K. C. EDA-NOCV Analysis of Carbene-Borylene Bonded Dinitrogen Complexes for Deeper Bonding Insight: A Fair Comparison with a Metal-Dinitrogen System. *J Comput Chem* **2022**, *43* (11), 757–777. https://doi.org/10.1002/jcc.26832.

(45) Boys, S. F.; Bernardi, F. The Calculation of Small Molecular Interactions by the Differences of Separate Total Energies. Some Procedures with Reduced Errors. *Mol Phys* **1970**, *19* (4), 553–566. https://doi.org/10.1080/00268977000101561.

(46) Vannice, M. A. *Kinetics of Catalytic Reactions*, 1st ed.; Springer, Ed.; Springer New York, NY: New York, 2005. https://doi.org/https://doi.org/10.1007/b136380.

(47) SING, K. S. W.; EVERETT, D. H.; HAUL, R. A. W.; MOSCOU, L.; PIEROTTI, R. A.; ROUQUEROL, J.; SIEMIENIEWSKA, T. Reporting Physisoption Data for Gas/Solid Systems with Special Reference to the Determination of Surface Area and Porosity. *Pure & Appl. Chem.* **1985**, *57* (4), 603–619.

(48) Han, Y.; Liu, M.; Li, K.; Zuo, Y.; Wei, Y.; Xu, S.; Zhang, G.; Song, C.; Zhang, Z.; Guo, X. Facile Synthesis of Morphology and Size-Controlled Zirconium Metal–Organic FrameworkUiO-66: The Role of Hydrofluoric Acid in Crystallization. *CrystEngComm* **2015**, *17*, 6434. https://doi.org/10.1039/c5ce00729a.

View Article Online
DOI: 10.1039/D5DT00494B

(49) Camu, E.; Pazo, C.; Becerra, D.; Hidalgo-Rosa, Y.; Paez-Hernandez, D.; Zarate, X.; Schott, E.; Escalona, N. A New Approach to the Mechanism for the Acetalization of Benzaldehyde over MOF Catalysts †. *New J. Chem* **2020**, *44*, 14865. https://doi.org/10.1039/d0nj02416c.

(50) Rogge, S. M. J.; Yot, P. G.; Jacobsen, J.; Muniz-Miranda, F.; Vandenbrande, S.; Gosch, J.; Ortiz, V.; Collings, I. E.; Devautour-Vinot, S.; Maurin, G.; Stock, N.; Van Speybroeck, V. Charting the Metal-Dependent High-Pressure Stability of Bimetallic UiO-66 Materials. *ACS Mater Lett* **2020**, *2* (4), 438–445. https://doi.org/10.1021/acsmaterialslett.0c00042.

(51) Lammert, M.; Wharmby, M. T.; Smolders, S.; Bueken, B.; Lieb, A.; Lomachenko, K. A.; Vos, D. de; Stock, N. Cerium-Based Metal Organic Frameworks with UiO-66 Architecture: Synthesis, Properties and Redox Catalytic Activity. *Chemical Communications* **2015**, *51* (63), 12578–12581. https://doi.org/10.1039/C5CC02606G.

(52) Valenzano, L.; Civalleri, B.; Chavan, S.; Bordiga, S.; Nilsen, M. H.; Jakobsen, S.; Lillerud, K. P.; Lamberti, C. Disclosing the Complex Structure of UiO-66 Metal Organic Framework: A Synergic Combination of Experiment and Theory. *Chem. Mater* **2011**, *23*, 1700–1718. https://doi.org/10.1021/cm1022882.

(53) Destefano, M. R.; Islamoglu, T.; Garibay, S. J.; Hupp, J. T.; Farha, O. K. Room-Temperature Synthesis of UiO-66 and Thermal Modulation of Densities of Defect Sites. **2017**. https://doi.org/10.1021/acs.chemmater.6b05115.

(54) Valenzano, L.; Civalleri, B.; Chavan, S.; Bordiga, S.; Nilsen, M. H.; Jakobsen, S.; Lillerud, K. P.; Lamberti, C. Disclosing the Complex Structure of UiO-66 Metal Organic Framework: A Synergic Combination of Experiment and Theory. *Chem. Mater.* **2011**, *23* (7), 1700–1718. https://doi.org/10.1021/cm1022882.

(55) Topsøe, N. Y.; Pedersen, K.; Derouane, E. G. Infrared and Temperature-Programmed Desorption Study of the Acidic Properties of ZSM-5-Type Zeolites. *J Catal* **1981**, *70* (1), 41–52. https://doi.org/10.1016/0021-9517(81)90315-8.

(56) Jiang, X.; Li, S.; He, S.; Bai, Y.; Shao, L. Interface Manipulation of CO2–Philic Composite Membranes Containing Designed UiO-66 Derivatives towards Highly Efficient CO2 Capture. *J Mater Chem A Mater* **2018**, *6* (31), 15064–15073. https://doi.org/10.1039/C8TA03872D.

View Article Online
DOI: 10.1039/D5DT00494B

(57) Asgari, M.; Jawahery, S.; Bloch, E. D.; Hudson, M. R.; Flacau, R.; Vlaisavljevich, B.; Long, J. R.; Brown, C. M.; Queen, W. L. An Experimental and Computational Study of CO2 Adsorption in the Sodalite-Type M-BTT (M = Cr, Mn, Fe, Cu) Metal-Organic Frameworks Featuring Open Metal Sites. *Chem Sci* **2018**, *9* (20), 4579–4588. https://doi.org/10.1039/c8sc00971f.

(58) Mitoraj, M. P.; Michalak, A. Theoretical Description of Halogen Bonding - An Insight Based on the Natural Orbitals for Chemical Valence Combined with the Extended-Transition- State Method (ETS-NOCV). *J Mol Model* **2013**, *19* (11), 4681–4688. https://doi.org/10.1007/s00894-012-1474-4.

(59) Paterová, I.; Vyskočilová, E.; Červený, L. Two-Step Preparation of Benzylacetone. *Top Catal* **2012**, *55* (11–13), 873–879. https://doi.org/10.1007/s11244-012-9853-8.

(60) Rao, K. K.; Gravelle, M.; Valente, J. S.; Figueras, F. Activation of Mg–Al Hydrotalcite Catalysts for Aldol Condensation Reactions. *J Catal* **1998**, *173* (1), 115–121. https://doi.org/10.1006/jcat.1997.1878.

(61) Sun, R.; Han, C.; Xu, J. A Green Synthesis Approach toward Large-Scale Production of Benzalacetone *via* Claisen–Schmidt Condensation. *RSC Adv* **2022**, *12* (45), 29240–29245. https://doi.org/10.1039/D2RA05320A.

(62) Ghosh, S.; Acharyya, S. S.; Yoshida, Y.; Kaneko, T.; Iwasawa, Y.; Sasaki, T. Nontraditional Aldol Condensation Performance of Highly Efficient and Reusable Cs^+ Single Sites in β-Zeolite Channels. *ACS Appl Mater Interfaces* **2022**, *14* (16), 18464–18475. https://doi.org/10.1021/acsami.2c01312.

(63) Pazo-Carballo, C.; Blanco, E.; Camu, E.; Leiva, A.; Hidalgo-Rosa, Y.; Zarate, X.; Dongil, A. B.; Schott, E.; Escalona, N. Theoretical and Experimental Study for Cross-Coupling Aldol Condensation over Mono- and Bimetallic UiO-66 Nanocatalysts. *ACS Appl Nano Mater* **2023**, *6* (7), 5422–5433. https://doi.org/10.1021/acsanm.2c05555.

(64) Rojas-Buzo, S.; García-García, P.; Corma, A. Catalytic Transfer Hydrogenation of Biomass-Derived Carbonyls over Hafnium-Based Metal-Organic Frameworks. *ChemSusChem* **2018**, *11* (2), 432–438. https://doi.org/10.1002/cssc.201701708.

(65) Rojas-Buzo, S.; García-García, P.; Corma, A. Hf-Based Metal-Organic Frameworks as Acid-Base Catalysts for the Transformation of Biomass-Derived Furanic Compounds into Chemicals. *Green Chemistry* **2018**, *20* (13), 3081–3091. https://doi.org/10.1039/c8gc00806j.

View Article Online
DOI: 10.1039/D5DT00494B

(66) Climent, M. J.; Corma, A.; Fornés, V.; Guil-Lopez, R.; Iborra, S. Aldol Condensations on Solid Catalysts: A Cooperative Effect between Weak Acid and Base Sites. *Adv Synth Catal* **2002**, *344* (10), 1090–1096. https://doi.org/10.1002/1615-4169(200212)344:10<1090::AID-ADSC1090>3.0.CO;2-X.

(67) Li, G.; Wang, B.; Resasco, D. E. Oxide-Catalyzed Self- and Cross-Condensation of Cycloketones. Kinetically Relevant Steps That Determine Product Distribution. *J Catal* **2020**, *391*, 163–174. https://doi.org/10.1016/j.jcat.2020.07.019.

View Article Online
DOI: 10.1039/D5DT00494B

The data supporting this article have been included as part of the Supplementary Information.